Cartography of a multistable system using support vector machines, applied to a clarinet model

Tom Colinot, Nathan Szwarcberg, Christophe Vergez, Samy Missoum

Cartography of a multistable system using support vector machines, applied to a clarinet model

Tom Colinot[1,2*], Nathan Szwarcberg[1,2], Christophe Vergez[2], Samy Missoum[3]

[1*]Buffet Crampon, 5, rue Maurice Berteaux, Mantes-la-Ville, 78711, France.
[2]Aix Marseille Univ, CNRS, Centrale Med, LMA, 4, Impasse Nikola Tesla, Marseille, 13013, France.
[3]Department of Aerospace and Mechanical Engineering, University of Arizona, Tucson, 85721, AZ, United States of America.

*Corresponding author(s). E-mail(s): tom.colinot@buffetcrampon.com;
Contributing authors: nathan.szwarcberg@buffetcrampon.com; vergez@lma.cnrs-mrs.fr; smissoum@arizona.edu;

Abstract

This paper presents a method to map out the behavior of a multistable dynamical system. The method outputs the boundaries of the stability regions of each multistable regime in the space of system parameters. Boundaries are produced by Support Vector Machines models. Adaptive sampling is used to improve speed and generalization to high dimensions. The method is general to any dynamical system with distinguishable multistable regimes. It is applied to a clarinet model with four distinct regimes (equilibrium and three distinct periodic notes). The cartography shows that, on the highest fingerings, the simple clarinet model only favors the expected note for very narrow ranges of reed parameters.

Keywords: Multistability, Support Vector Machines, Musical Acoustics, Clarinet

1 Introduction

Multistability is the coexistence of several stable regimes for a single set of values of the parameters of a system. It is inherent to the behavior of many dynamical systems, such as biological models [1], neural networks [2], or ecological models [3]. In practice, multistability causes unpredictability in the system's behavior, when considering the relation between the value of the system parameters and the observed regime. For example, a multistable musical instrument model is not guaranteed to play the desired note. On the one hand, this behavior can be considered desirable, because it translates a realistic difficulty in playing the acoustic instrument. On the other hand, it can be considered undesirable, if the user wants the model to reliably play the desired notes. In both cases, it is interesting to outline the multistability regions in the control parameter space. They can then be avoided or favored depending on the use case.

Self-sustained musical instruments models are largely multistable. Evidence has been provided for violin [4], brass instruments [5, 6], and woodwinds such as saxophones [7] or clarinet-like instruments [8]. When playing an instrument, the musician often wants to obtain a given regime.

In the case of multistability, that is not guaranteed, as another regime can appear and be maintained instead of the desired one. A sure way to obtain a given regime is to find a monostability region, i.e. control parameter values that necessarily lead to a given regime. Maps referencing stable regimes throughout the control parameter space can be used to better understand player strategies, or to ensure a certain regime is produced if the instrument model is used in sound synthesis [9]. Producing these maps is challenging, because there are often many control parameters, and potentially many multistable regimes. Notably, the traditional approaches based on bifurcation diagrams do not scale well in high dimensions. Another traditional method is Linear Stability Analysis which is easily applied in high dimensions [10]. However, this method give little information beyond the loss of stability of the non-oscillating regime.

The present study characterizes the stability zone of each multistable regime in the control parameter space. Classical *carpet bombing* approaches, where the space is meshed in a systematic manner, or Monte Carlo methods where new samples are chosen randomly, fall apart when the dimension of the space increases.

The presented method relies on Support Vector Machines and adaptive sampling to estimate the boundary of the stability zones. Using a small number of points as initialization, new samples are added where needed by Explicit Design Space Decomposition (EDSD) [11]. This allows the method to work with several control parameter space dimensions as well as multistable regimes to study.

Note that a complete study of a multistable system involves mapping out the basin of attraction of each multistable regime, i.e. the initial conditions which lead to each regime, for each value of the control parameters. This aspect of the study is not considered here as it increases the dimension of the problem by the number of variables of system.

First, we present the simple clarinet model and the expected oscillation regimes. Then, the cartography method is detailed, especially the initialization and the precautions to take when testing a new point in the parameter space. The method is then applied to the space of the control parameters of the clarinet (blowing, lip force, reed parameters) in increasing dimension.

2 Preliminary: a multistable woodwind model

2.1 The clarinet model

This work treats a simple modal clarinet model, similar to that used in [10, 12, 13]. The resonator is modeled by a modal formalism. The modal pressures time-derivative are given by

$$\dot{p}_k = C_k u + s_k p_k \tag{1}$$

and the pressure is computed as the sum of their real part

$$p = 2\sum_{k=1}^{N_m} \mathrm{Re}(p_k) \tag{2}$$

The number of modes is set at $N_m = 3$, and C_k and s_k are due to modal analysis on a measured impedance [14]. The flow rate at the input of the resonator is classically given as a function of the pressure p as

$$u = \zeta[x+1]^+ \mathrm{sign}(\gamma - p)\sqrt{|\gamma - p|}$$

where the two control parameters γ and ζ respectively depend on the blowing pressure and lip force of the musician, and x is the reed position. The notation $[x+1]^+ = max(x+1, 0)$ is the positive part of the reed opening. This characteristic is regularized by using the smooth function $\sqrt{.^2 + \eta}$ [15] instead of absolute values:

$$u = \zeta(\gamma - p)\frac{x + 1 + \sqrt{(x+1)^2 + \eta}}{2\left((\gamma - p)^2 + \eta\right)^{1/4}}. \tag{3}$$

The regularization parameter η is fixed at $\eta = 10^{-3}$. The reed position x is governed by a single degree-of-freedom oscillator

$$\ddot{x} + q_r\omega_r\dot{x} + \omega_r^2(x - p + \gamma) = 0, \tag{4}$$

with parameters q_r (damping) and ω_r (angular eigenfrequency). For this study, the reed damping q_r is set at 0.1, which is a rather low value. Here, the reed displacement is considered unaffected by

the mouthpiece rails, following the usual *ghost reed* simplification [16]. The integration of the differential system is performed using the Matlab built-in ODE45 routine [17] with the default tolerances and parameters.

2.2 Classifying clarinet regimes

In addition to the stable non-oscillating regime, the clarinet model produces several types of oscillation distinguished by their fundamental frequency. Each one can be tied to a single mode of the resonator, and they are referred to as first, second and third register sounds (depending on the index of the corresponding mode). The fundamental angular frequency of each register is close to $\Im(s_k)$. A robust way to label each regime on the clarinet is a comparison of the amplitude of the modal pressures p_k. The greatest amplitude gives the current register. Figure 1 illustrates the non-oscillating and periodic regimes. These signals are obtained with constant blowing pressure $\gamma = 0.4$ and reed opening parameter $\zeta = 0.4$. The reed eigenfrequency ω_r increases and as it approaches the modal eigenfrequencies the corresponding register is produced. When a new register appears, the corresponding modal pressure greatly increases while the two others decrease.

3 Two-dimensional multistable cartography

3.1 The support vector machines and adaptive sampling (EDSD)

A Support Vector Machine (SVM) model estimates the boundary between regions of qualitatively different behavior in the control parameter space. We use the CODES toolbox [11], which builds and trains SVM models. It also includes adaptive sampling tools. The CVT (Central Voronoi Tesselation) method provides an initial set of points to start the SVM training. The EDSD (Explicit Design Space Decomposition) method selects relevant new points in the space to test at each iteration. These points are used to refine the SVM model.

In our case, the regions of interest are the regions of stability of each clarinet regime (non-oscillating and first, second and third register).

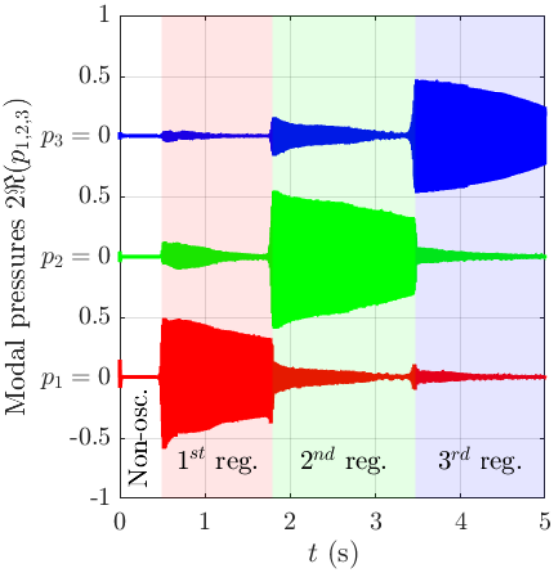

Fig. 1 Regimes of the clarinet model for a single fingering. Control parameters: $\gamma = 0.4$, $\zeta = 0.4$, ω_r linearly varying from 12 to 12000 rad.s^{-1})

These stability regions overlap because the clarinet model is multistable. Therefore, it is necessary to have a separate SVM model for each regime. For each SVM model, samples labeled *positive* are the points where the corresponding regime is stable. For samples labeled *negative*, the corresponding regime loses its stability, either by becoming unstable or by disappearing.

3.2 Initialization for a clarinet

The initialization process is schematized in Figure 2.

First, a CVT grid of points is produced in the parameter space. We produce initial samples through time-domain integration of the model. For each sample, a new integration is launched with null initial conditions. During these integrations, the control parameters are constant. The permanent regime that is observed at the end of each integration is considered stable. This information then leads to each labeling sample as positive or negative, depending on the SVM model (i.e. the regime under focus). This process is illustrated in Figure 2. Figure 2 (a) shows the regime obtained at the end of the time integration procedures, and they are labeled differently in (b) and (c). Indeed,

in Figure 2 (b) the focus is on the stability zone of the non-oscillating regime, and in Figure 2 (c) the focus is on the stability zone of the first register. Similar labeling is carried out to initialize the SVM models giving the frontiers of the regions where regimes 2 and 3 are stable.

It is crucial for initialization samples to avoid multistability zones between the regime of interest and the others. Otherwise, the learning starts with spurious negative samples. This requires knowledge of the system, so that initialization samples avoid these regions.

For the clarinet model, the Hopf bifurcations giving birth to each periodic regime are almost always direct [18] and near $\gamma = 1/3$. This means that there is no multistability regions between the equilibrium and the periodic regimes around these Hopf bifurcations. We also know that Hopf bifurcations in ζ are direct [15]. However, it is not the case in all the parameter space. For γ beyond $\gamma_M^i = 1$ the periodic branches stay stable before they encounter a fold bifurcation, and end in a Hopf bifurcation near $\gamma = 1$. This means that $\gamma > 1$ is a potential multistability region between the non-oscillating and the oscillating regimes. Figure 2 (a) highlights in yellow the safe region of the parameter space where the CVT grid is created. This region is free of multistability for the non-oscillating regime, which makes all the samples in it suitable for initializing the non-oscillating SVM model.

The situation is different for the oscillating regimes, which are potentially multistable. To produce a clean initialization set for oscillating SVM models, the oscillating samples that are not the regimes of interest are deleted. This yields a new initialization set, such as the one displayed in Figure 2 (c) for the first register.

The SVM models must outline the stability regions of each regime. When a new point is added, one cannot simply launch a time integration with arbitrary initial conditions (as is the case for the initialization samples). This is because of multistability. Even if the regime of interest is stable at the tested point, arbitrary initial conditions risk leading to another regime. This would constitute a misclassification. To avoid these errors, the time integration starts from the closest known positive sample, with initial conditions corresponding to

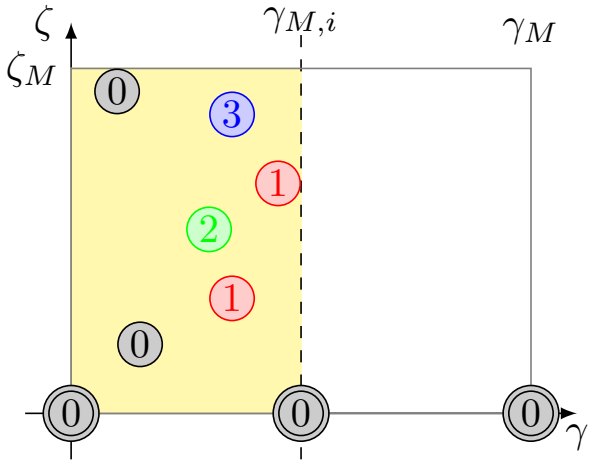

(a) All initialization samples

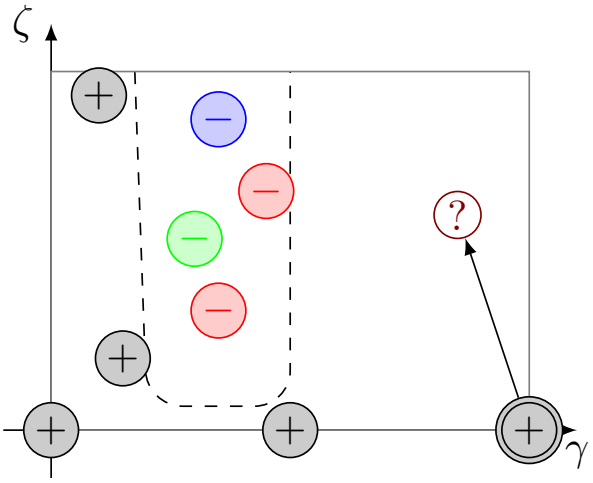

(b) Focus on non-oscillating regime

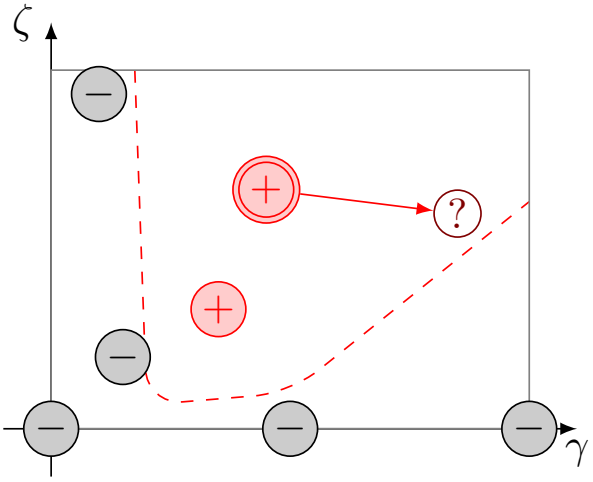

(c) Focus on first register regime

Fig. 2 Initialization of the Support Vector Machines problem. (a) all initial samples. Initial CVT range: yellow area. Added known non-oscillating samples (0). First new sample evaluation for (b) the non-oscillating regime and (c) the first register. Positive samples (+), negative samples (−), new sample (?), closest positive sample (+), evaluation trajectory →. Expected stability limits: dashed lines. In (c), the oscillating samples not belonging to the register of interest are removed.

the established regime of interest. This is schematized in Figure 2 (b) and (c). This way, if the regime of interest is stable on the path until the new sample, the new sample is then classified as positive. If, on the contrary, the regime loses its stability somewhere along the path, the new sample is classified as negative. To ensure whether the regime stays stable on the new sample, some time is spent on the new sample without varying the control parameters.

Note that the method can fail if the stability zone is concave or non-connected. This can be mitigated by adding samples, notably in the initialization. In the clarinet model, this poses a problem for the non oscillating regime. Three particular initial samples are added where the non oscillating regime is known to be stable, for $\zeta = 0$ and $\gamma = 0$, $\gamma = 1$ and $\gamma = \gamma_M$. They are highlighted by double circles on Figure 2 (a). Their use appears in Figure 2 (b). To test the new sample, the time integration starts from the positive sample at $(\gamma_M, 0)$. If the three particular samples at $\zeta = 0$ did not exist, the time integration would have to start from one of the positive samples at $\gamma < 1$ and $\zeta > 0$. The path would then cross the region where the non oscillating regime is unstable, and the new sample would be misclassified as negative.

To assess the ability of the SVM model to determine the stability zones of the different regimes, a validation set is constructed from the initialization points. Figure 3 schematizes the construction process. For each initialization point in the parameter space, its components along each dimension are varied one after the other by time integration, in both positive and negative directions. For initialization points located on the $\zeta = 0$ axis, variations along γ are not performed, since the system is known to be monostable in the non-oscillating regime when $\zeta = 0$. The same applies to the points on the $\gamma = 0$ axis and the variation of ζ. Adding these trivial points to the validation set would tend to make the test too simple, and thus overestimate model convergence. These variations are performed by small steps, e.g. $1/20$ of the dimension range (the step in Figure 3 is different, for illustrative purposes). One time integration lasts $2\Delta t$. During the first Δt, the component to be varied evolves linearly to its final value. It is then kept constant for the same duration Δt.

The progression along a dimension persists until it reaches one of the boundaries of the parameter space, or when the regime of the initialization point loses its stability. In that case, the last sample is then stored as negative in the validation set and the time-integration stops. Any further negative points run the risk of being misclassified as a result of multistability. There are as many validation sets as regimes identified during the initialization procedure. When evaluating the performance of the model, it should be noted that reaching 100% accuracy is made very difficult by dynamical bifurcation phenomena. However, the validation set signals two possible failures of the model. Firstly, since new samples depend on the existing samples, any misclassification propagates with potentially dramatic effect. This is especially true for false positives which can be taken as starting points for subsequent integrations. Secondly, as mentioned earlier, the method is vulnerable to concave or disconnected stability zones. Comparison of the SVM model to the validation set signals any large scale omission, notably of a disconnected stability region.

This procedure of construction is designed to be generalized easily in higher dimension. While varying a single parameter at a time may seem naive, it makes the results easier to interpret and to compare to thresholds obtained by classical methods such as continuation.

3.3 Result: amplitude surfaces with stability boundaries

The first application of the method is to map out a two-dimensional parameter space, such as (γ, ζ). This parameter choice for woodwinds has been made in both experimental studies [19–21] and numerical studies [15, 22]. The results can also be compared with linear stability analysis [23].

Rather than just outlining the stability zones, we use the gathered data to approximate the amplitude of the stable periodic regimes. An interpolation is realized on the non uniform grid constituted by the SVM samples [24]. The amplitude of the regimes is linked to the loudness of the radiated sound. This is especially interesting on the edges of the stability regions. If the amplitude tends towards zero, it indicates that the regime can be played arbitrarily softly. In the opposite case, it can indicate that the softest nuances are

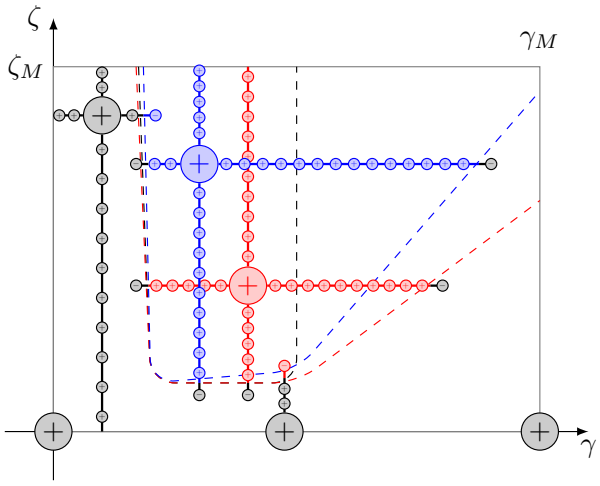

Fig. 3 Construction of the validation set. Positive samples (+), negative samples (−). Colors correspond to the regime of interest : black for non-oscillating, red for first register, blue for third register. Bigger nodes are initial samples and smaller nodes along thick lines constitute the samples validation set. Schematic stability limits: dashed lines.

not permitted with this regime. These considerations are linked to the direct or inverse nature of the Hopf bifurcations [18, 25]. The same could be done with another descriptor such as fundamental frequency.

The cartography in the (γ, ζ) plane based on the four SVM models is displayed in Figure 4. The fingering is the lowest of the clarinet (written E2, heard D2, approximately 146.8 Hz for the first register regime).

The reed parameters are picked so that the behavior of the model is quite rich. The angular eigenfrequency of the reed is $\omega_r = 2\pi \times 1100$ rad.s^{-1}, which is higher than the third modal frequency of $\Im(s_3) = 2\pi \times 706.4$ rad.s^{-1}. This makes the three different oscillating regimes possible to obtain (see Section 4 for further discussion). A rather low reed damping $q_r = 0.3$ also favors the apparition of second and third register regimes.

The range of the cartography is $\gamma \in [0; 4]$ and $\zeta \in [0.01; 1.7]$. This largely encompasses parameter value choices made in past numerical studies on the clarinet [26, 27]. Figure 4 shows that monostability (i.e. only one stable regime) is very rare throughout the parameter space. It happens mainly for the lowest values of γ and ζ where only the non oscillating regime is stable. For a majority of the space where $\gamma > 1$, the four regimes

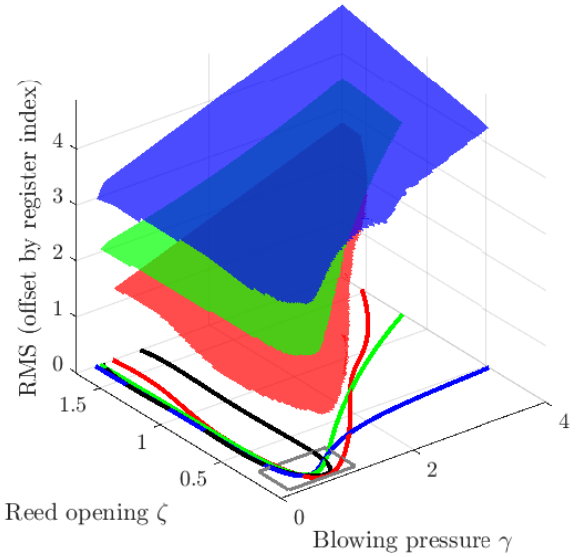

(a)

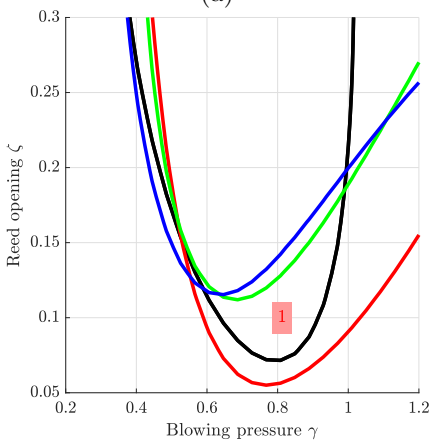

(b) Zoom around first register monostability

Fig. 4 (a) Multistable cartography for fingering written E2: RMS pressure vs. γ and ζ, within the limits of stability of each regime (red: first, green: second and blue: third register). Surfaces are vertically offset by 1, 2 and 3 (respectively) for clarity. The lines on the horizontal plane indicate the limits of stability (projected boundaries of the first, second and third register surfaces in colors, and limit of stability of the non-oscillating regime in black). The gray rectangle is zoomed on in (b). (b) Boundaries in the (γ, ζ) plane around the first register monostability region (highlighted by a red 1).

are stable. For $\gamma < 1$, it is more common to have all three oscillating regimes stable than two, and very rarely is only one regime stable. Figure 4 (b) shows that it only happens for a very low ζ and γ between 0.6 and 1. The oscillating regime that is monostable in that case is the first register. This

is the regime that is expected to sound for this fingering. With these reed parameters, ensuring that this regime appears seems very difficult. It requires either aiming precisely at the region where it is monostable, or leading the system into the first register's basin of attraction in a multistability zone. Basins of attraction for musical instrument models is only an emerging topic [7, 28, 29], and there is no evidence that musicians are able to target a specific region of the phase space of a system.

The SVM model does not provide proof as to the direct or inverse nature of the Hopf bifurcations. Some clues are contained in the amplitude at the boundary between the stability region of an oscillating regime. There is also a decisive clue in the distance between the non-oscillating stability limit. Figure 4 shows that the non-oscillating limit matches that of the third register, except for very low reed opening ζ. The amplitude of the third register regime also starts from an almost null value (the surface on Figure 4 begins around 3, because it is offset by the register index). Both of these facts together strongly point to a direct Hopf bifurcation: oscillations of arbitrarily low amplitude can be obtained near the threshold where the non-oscillating regime loses its stability. This is tested via time integration in Appendix A.

4 Cartography in higher dimensions

The second endeavor deals with the tree-dimensional space $(\gamma, \zeta, \omega_r)$. The reed damping remains low at $q_r = 0.2$. In this space, we choose to limit the study to $\gamma \in [0.05; 0.98]$, $\zeta \in [0.01; 0.5]$ and $\omega_r \in 2\pi \times [100; 3000]$ rad.s^{-1}. The domain in blowing pressure γ and ζ is comparable to that used in [10, 12, 13]. These three papers study simple models of clarinet very similar to the present one. They tackle its oscillation thresholds, which is a particular case of stability zone boundary. The present results can therefore be seen as an extension of these papers.

Fingerings A2, E4, and C♯5 serve as examples in this section. These fingerings each have a different expected register, indicated by their name: for A2, players expect the first register, for E4 the second and for C♯5 the third. In order to favor the higher registers, the player unplugs upstream holes while leaving the downstream part of the tonehole lattice unaffected. Figure 5 shows the acoustical input impedance for these fingerings. The peaks of the impedance curve signal the modes of the resonator. Their height, width and frequency condition the playable notes. Here, except for the first register fingering A2, the peak corresponding to the expected register is not taller than the others. For the fingerings E4 and C♯5 respectively, the first and second peak are rather disturbed in frequency by the opening of upstream holes. The tools developed in this article examine how this modification of the impedance affects regime stability zones. In particular, one could assume that the expected regime dominates the others.

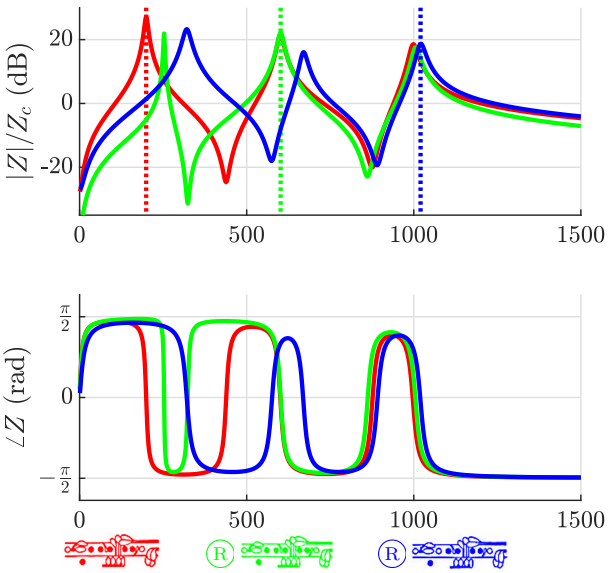

Fig. 5 Acoustical input impedances for fingerings A2 (red), E5 (green), and C♯6 (blue), and fingering layouts in corresponding colors. The symbol Ⓡ indicates that the register key is pressed.

Figure 6 displays the multistable cartography for the three studied fingerings. We focus first on Figure 6 (a), for the first register fingering (A2). As for the E2 fingering of Figure 4, multistability is pervasive and encompasses most of the control parameter space.

Figure 6 shows the stability regions for each regime. Comparison of the SVM prediction to the validation set returns values between 85% and 95% of correct answers. This is deemed satisfactory: no disconnected regions of stability are

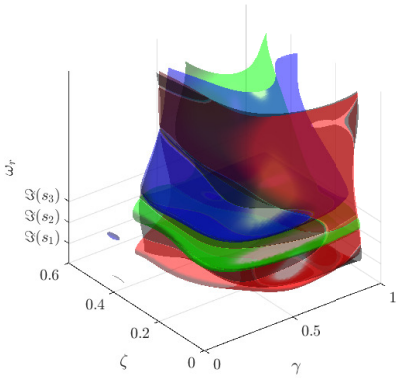

(a) A2:

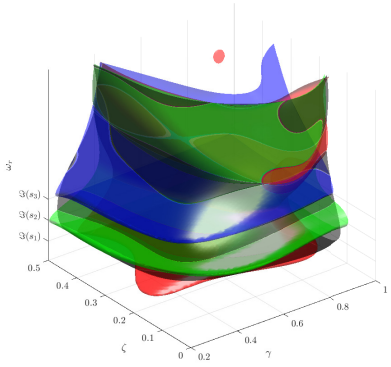

(b) E5: Ⓡ

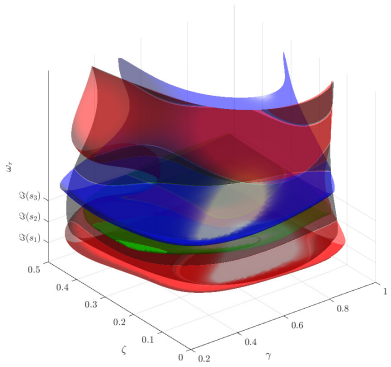

(c) C♯6: Ⓡ

Fig. 6 Limits of stability in the $(\gamma, \zeta, \omega_r)$ space. Non-oscillating regime (black), first (red) second (green) and third (blue) registers. Fingerings are written A2 (a), E5 (b), and C♯6 (c) with associated tablature (Ⓡsignals a pressed register key). Ticks in the ω_r axis mark the three modal frequencies $\Im(s_{1,2,3})$.

omitted. There are monostable regions, notably when the reed eigenfrequency ω_r is low. For $\omega_r = \omega_r^{min}$, only the non-oscillating regime is stable. This feature is also shown on the two-dimensional section at $\zeta = 0.2$ of Figure 7. For $\Im(s_1) < \omega_r < \Im(s_2)$, only the first register regime is stable. This region is interesting as the model can only produce silence or the expected regime throughout the (γ, ζ) plane. This result can also be deduced from the considerations on oscillating thresholds provided in [12]. When $\omega_r \simeq \Im(s_1)$, the stability region of the first register bulges outward. This is because of the low value of the reed damping q_r. Similar bulges occur when $\omega_r \simeq \Im(s_2)$ for the second register and when $\omega_r \simeq \Im(s_3)$ for the third register. This shape is announced in [13] and [10]. However, it appears that the bulges in our study outgrow the limit of stability of the non-oscillating regime, which indicates an inverse Hopf bifurcation. The limit of stability is then classically a saddle-node bifurcation, which cannot be detected by mere linear stability analysis. Figure 7 shows a two dimensional section of the stability zones along the plane $\zeta = 0.2$. Note that Figure 7 reuses the SVM models trained in three dimensions. Figure 7 shows small, arrow-shaped white regions (around $\gamma = 0.4$) that do not seem to belong to any stability regions. Specific time-domain integration in these zones, not depicted here for brevity, show that they are monostable non-oscillating regime. They should be part of the black region. In fact, the region outlined by the SVM has relatively smooth edges by construction of the gaussian kernel. Describing sharp angles requires significantly more samples, or different parameters for the kernel which degrades the performance of the model in other parts of the parameter space.

For $\omega_r >> \Im(s_3)$, the stability zones vary less, with the first register being the outer surface. This region of high ω_r seems to be the most relevant in practice. Experimental studies [30] find reed eigenfrequencies between 2 kHz and 3.5 kHz, higher than the third mode (around 1.1 kHz here). For the first register fingering A2, the second and third register stability zones seem largely inside of the first register zone. In particular, there is a large monostability zone of the first register at high ω_r for $\zeta < 0.25$. This monostability can be seen on Figure 7. This feature could indicate a clear dominance of the expected first register regime for

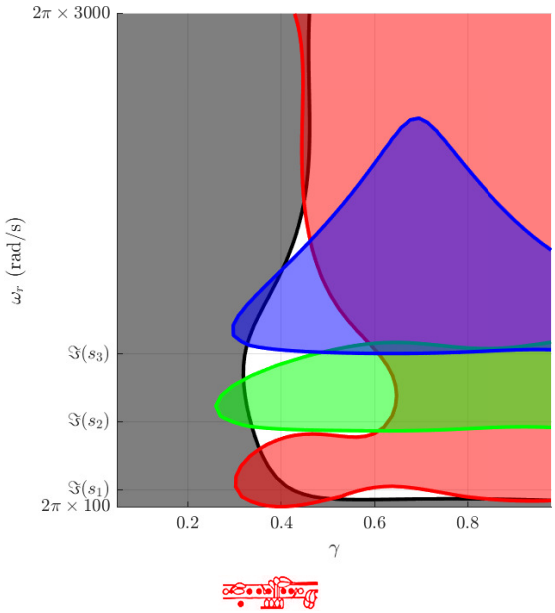

Fig. 7 Stability regions for $\zeta = 0.2$. Non-oscillating regime (black), first (red) second (green) and third (blue) registers. Fingering: written A2.

this fingering. This conclusion cannot be reached from the linear stability analysis of previous work, where oscillation thresholds of all registers tend to very similar values for high reed eigenfrequency.

For the second register fingering E4 in Figure 6 (b), the first register stability zone shrinks, especially in the region where $\omega_r \simeq \Im(s_1)$. This matches the function of pressing the register key: hindering the production of the first register. However, for high reed eigenfrequency ω_r, the first and second register stability zones are very close together. The second register is mostly the outer limit, but there is only a very slim zone of monostability. The third register surface is also larger than for the A2 fingering. All of this means that this fingering is almost never guaranteed to produce the expected second register. The largest monostability zone for the second register is obtained at the bulge around $\omega_r \simeq \Im(s_2)$.

For fingering C♯5 in Figure 6 (c), the expected third register seems even more difficult to ensure. Except for $\omega_r \simeq \Im(s_3)$ the third register multistability zone never outgrows the two others. At high ω_r values, the first register stability zone is the largest. Although narrower than for the first register fingering A2, there is a clear monostability zone for the first register before the third register becomes stable again. However, the second register stability zone is shrunk to the point where it disappears when $\omega_r > \Im(s_3)$. Multistability zones featuring the three oscillating regimes are rare for this fingering.

The fingerings can be compared quantitatively by computing the volume of each stability zone. The percentage of the parameter space that is occupied by each regime is summarized in Table 1. Each regime (in bold) occupy a larger volume for the fingering where it is expected than for the others. However, the differences can be very tenuous, especially in the case of the third register. The first register also occupies a similar volume for A2 and C♯5 (the first and third register fingering).

$q_r = 0.1$

	Non-osc	1^{st} reg	2^{nd} reg	3^{rd} reg
A2	44.7%	**38.5%**	20.2%	26.0%
E5	52.1%	26.8%	**38.1%**	28.1%
C♯6	51.2%	36.9%	7.2%	**27.6%**

$q_r = 0.2$ (all other figures)

	Non-osc	1^{st} reg	2^{nd} reg	3^{rd} reg
A2	50.0%	**46.2%**	17.9%	24.8%
E4	55.9%	33.8%	**37.5%**	25.7%
C♯5	54.9%	42.1%	5.93%	**26.0%**

$q_r = 0.5$

	Non-osc	1^{st} reg	2^{nd} reg	3^{rd} reg
A2	54.3%	**46.8%**	16.0%	15.0%
E5	61.2%	38.8%	**34.8%**	16.9%
C♯6	60.1%	41.0%	1.36%	**17.3%**

Table 1 Percentage of the parameter space $(\gamma, \zeta, \omega_r)$ occupied by the stability zones of each regime for the three studied fingerings (written A2, E4, C♯5). Values for the expected regime for each fingering are in bold.

The features of Figure 6 (b) and (c) and the results of Table 1 indicate the model is mostly unable to guarantee second and third register regime on the fingerings where it is expected. This feature translates to other values of q_r and η, and can therefore be called a feature of the model itself (given that the modal parameters are measured on a real clarinet). This lack in production of the second and third register puts into question the simple clarinet model used here. This type of model is widely accepted as correctly describing first register fingerings on the clarinet (such as A2) [26, 31]. However, it has very rarely been

used to simulate second and third register fingerings. This study offers some possible reasons. For the present clarinet model to produce second and third register regimes, one needs to set the reed eigenfrequency near the frequency of the corresponding mode. Players can impact the reed eigenfrequency, using their lip for example. However, it seems dubious that they would adapt it specifically to each fingering of the instrument. It is more probable that the present simple model fails to encapsulate a real instrument's behavior for high fingerings because a physical effect was abusively ignored. Nonlinear losses in the upstream holes of the instrument have been cited as a potential improvement in this direction [32–34]. These losses are a difficult topic, which is beyond the scope of the present work.

5 Discussion: on linear stability analysis

Note that [10, 12, 13] deal with the oscillation threshold of a simplified clarinet model very close to the one studied here. They all aim to outline the region of existence of each regime, and map out which one emerges at the lowest blowing pressure γ as a function of the reed parameters. The present paper has similar aims, but studies stability zones instead of oscillation threshold, which entails two major consequences. Firstly, oscillation thresholds only give information for low-amplitude oscillation. Secondly, nothing guarantees an emerging regime to be stable anywhere, especially if the fixed point it emerges from is unstable. Therefore, the most informative oscillation threshold is the first one, as illustrated by [10] which devotes a lot of attention to the lowest oscillation threshold. In this paper, the locus of the first oscillation threshold is described by the SVM model attached to the non oscillating regime. The boundaries traced by the SVM models attached to oscillating regimes are zones of stability in which they can be obtained and maintained during a time-integration. Of course, the SVM models say nothing of the point at which solution branches emerge from fixed points. They also give no indication as to the relative probability of apparition of a given regime in multistability, which would require a study of the basins of attraction.

6 Conclusion

The stability zones of multistable dynamical systems can be mapped out using Support Vector Machines. The method generalizes to higher dimensions more straightforwardly than usual continuation methods, especially because of adaptive sampling. By accounting for multistability, it gives information that is hard to gather using classical carpet-bombing approaches. The initialization procedure requires some initial knowledge of the system: at least one monostability zone must be known *a priori*.

The method yields interesting conclusions on the behavior of a simple self-sustained musical instrument model. Firstly, it reinforces and expands upon previous results obtained by linear stability analysis. Secondly, the methods allows an exhaustive mapping of three-dimensional chunks of the control parameter space. This draws a strong conclusion on the inability of this model to reliably produce high register regimes, unless the reed is tuned to a particular mode of the resonator. Producing an exhaustive cartography of the control parameter space (4 dimensions here), or even of the 14 dimensions of the model including the modal parameters is attainable using the method, but the results would be rather tedious to assimilate.

Appendix A Direct Hopf bifurcation

Figure 4 hints at a direct Hopf bifurcation around $\gamma = 0.35$. A verification of this behavior is done by time integration. Figure A1 shows the results of the time integration for $\zeta = 0.4$. The figure was generated by increasing the blowing pressure γ by small steps, integrating until the permanent regime is reached for each value, and then decreasing it using the same values. This procedures allows to check for hysteresis. Figure A1 indicates that the third register is the one that appears in numerical integration, which confirms that it is the first to become stable when the non oscillating regime loses stability. Figure A1 also shows that the bifurcation is direct, as predicted: there is almost no hysteresis phenomenon. Only one point is different when γ increases or when it decreases, and the dynamics around the Hopf bifurcation are so slow that transients become

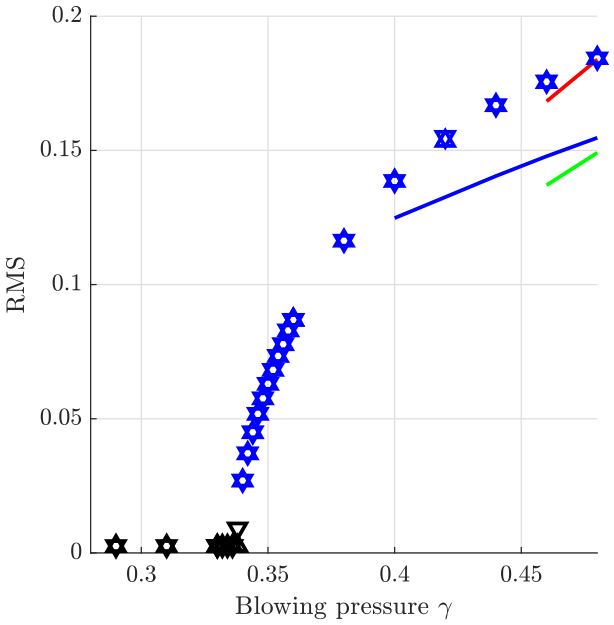

Fig. A1 Exploration of the behavior around the boundaries between stability regions for the non-oscillating and third register regime. Lines are cuts of the surfaces of figure 4. Upwards triangles are due to time-integration with increasing γ, downwards triangles with decreasing γ. Their color indicates the register (black : non oscillating, blue : third register).

indistinguishable from the permanent regime. The RMS amplitude of the SVM samples (plain line) does not fit exactly the one obtained by time integration (triangles) in that case, but remember that the RMS estimate is due to interpolation between points that can be relatively far away compared to the fine variations of γ and RMS value considered here.

Note that the direct nature of the Hopf bifurcation has a direct implication on the behavior of the model when used for real-time sound synthesis: setting the mouth pressure allows to play with arbitrarily low volumes. This example is also a reminder that the first stability threshold holds a particular significance since it is the one that is observed for slowly varying control parameters.

References

[1] Ozbudak, E.M., Thattai, M., Lim, H.N., Shraiman, B.I., Van Oudenaarden, A.: Multistability in the lactose utilization network of escherichia coli. Nature **427**(6976), 737–740 (2004)

[2] Cheng, C.-Y., Lin, K.-H., Shih, C.-W.: Multistability in recurrent neural networks. SIAM Journal on Applied Mathematics **66**(4), 1301–1320 (2006)

[3] Watson, A.J., Lovelock, J.E.: Biological homeostasis of the global environment: the parable of daisyworld. Tellus B: Chemical and Physical Meteorology **35**(4), 284–289 (1983)

[4] Schumacher, R., Woodhouse, J.: Computer modelling of violin playing. Contemporary Physics **36**(2), 79–92 (1995)

[5] Velut, L.: Contrôle par le musicien des régimes d'oscillation des instruments de la famille des cuivres: modélisation et mesures acoustiques, analyse du système dynamique. PhD thesis, Aix-Marseille (2016)

[6] Fréour, V., Guillot, L., Masuda, H., Tominaga, E., Tohgi, Y., Vergez, C., Cochelin, B., *et al.*: Numerical continuation of a physical model of brass instruments: Application to trumpet comparisons. The Journal of the Acoustical Society of America **148**(2), 748–758 (2020)

[7] Colinot, T., Vergez, C., Guillemain, P., Doc, J.-B.: Multistability of saxophone oscillation regimes and its influence on sound production. Acta Acustica **5**, 33 (2021)

[8] Tachibana, T., Takahashi, K.: Sounding mechanism of a cylindrical pipe fitted with a clarinet mouthpiece. Progress of Theoretical Physics **104**(2), 265–288 (2000)

[9] Chatziioannou, V., Pàmies-Vilà, M., Hofmann, A.: Physics-based playability maps for single-reed woodwind instruments. JASA Express Letters **4**(3) (2024)

[10] Karkar, S., Vergez, C., Cochelin, B.: Oscillation threshold of a clarinet model: A numerical continuation approach. The Journal of the Acoustical Society of America **131**(1), 698–707 (2012)

[11] Lacaze, S., Missoum, S.: CODES: A Toolbox

For Computational Design (2015)

[12] Wilson, T.A., Beavers, G.S.: Operating modes of the clarinet. The Journal of the Acoustical Society of America **56**(2), 653–658 (1974)

[13] Silva, F., Kergomard, J., Vergez, C., Gilbert, J.: Interaction of reed and acoustic resonator in clarinetlike systems. The Journal of the Acoustical Society of America **124**(5), 3284–3295 (2008)

[14] Ablitzer, F.: Peak-picking identification technique for modal expansion of input impedance of brass instruments. EDP Sciences (2021)

[15] Colinot, T.: Numerical simulation of woodwind dynamics: investigating nonlinear sound production behavior in saxophone-like instruments. PhD thesis, Aix-Marseille Université (2020)

[16] Colinot, T., Guillot, L., Vergez, C., Guillemain, P., Doc, J.-B., Cochelin, B.: Influence of the "ghost reed" simplification of the bifurcation diagram of a saxophone model. Acta Acustica united with Acustica **105**(6), 1291–1294 (2019)

[17] Shampine, L.F., Reichelt, M.W.: The matlab ode suite. SIAM journal on scientific computing **18**(1), 1–22 (1997)

[18] Dalmont, J.-P., Gilbert, J., Kergomard, J.: Reed instruments, from small to large amplitude periodic oscillations and the helmholtz motion analogy. Acta Acustica united with Acustica **86**(4), 671–684 (2000)

[19] Dalmont, J.-P., Frappe, C.: Oscillation and extinction thresholds of the clarinet: Comparison of analytical results and experiments. The Journal of the Acoustical Society of America **122**(2), 1173–1179 (2007)

[20] Almeida, A., George, D., Smith, J., Wolfe, J.: The clarinet: How blowing pressure, lip force, lip position and reed "hardness" affect pitch, sound level, and spectrum. The Journal of the Acoustical Society of America **134**(3), 2247–2255 (2013)

[21] Doc, J.-B., Vergez, C.: Oscillation regimes produced by an alto saxophone: Influence of the control parameters and the bore inharmonicity. The Journal of the Acoustical Society of America **137**(4), 1756–1765 (2015)

[22] Taillard, P.-A., Kergomard, J., Laloë, F.: Iterated maps for clarinet-like systems. Nonlinear dynamics **62**, 253–271 (2010)

[23] Grand, N., Gilbert, J., Laloë, F.: Oscillation threshold of woodwind instruments. Acta Acustica united with Acustica **83**(1), 137–151 (1997)

[24] Amidror, I.: Scattered data interpolation methods for electronic imaging systems: a survey. Journal of electronic imaging **11**(2), 157–176 (2002)

[25] Bouasse, H.: Instruments À vent. Impr. Delagrave, ??? (1929)

[26] Guillemain, P., Kergomard, J., Voinier, T.: Real-time synthesis of clarinet-like instruments using digital impedance models. The Journal of the Acoustical Society of America **118**(1), 483–494 (2005)

[27] Taillard, P.-A., Silva, F., Guillemain, P., Kergomard, J.: Modal analysis of the input impedance of wind instruments. application to the sound synthesis of a clarinet. Applied Acoustics **141**, 271–280 (2018)

[28] Terrien, S., Bergeot, B., Vergez, C.: De la stabilité locale à la stabilité globale: application à un modèle simple d'instrument à anche. In: 16ème Congrès Français d'Acoustique, CFA2022 (2022)

[29] Brzeski, P., Belardinelli, P., Lenci, S., Perlikowski, P.: Revealing compactness of basins of attraction of multi-dof dynamical systems. Mechanical Systems and Signal Processing **111**, 348–361 (2018)

[30] Chatziioannou, V., Schmutzhard, S., Pàmies-Vilà, M., Hofmann, A.: Investigating clarinet articulation using a physical model and

an artificial blowing machine. Acta Acustica United with Acustica **105**(4), 682–694 (2019)

[31] Chatziioannou, V., Walstijn, M.: Estimation of clarinet reed parameters by inverse modelling. Acta Acustica united with Acustica **98**(4), 629–639 (2012)

[32] Ducasse, E.: A physical model of a single-reed wind instrument including actions of the player. Computer Music Journal **27**(1), 59–70 (2003)

[33] Guillemain, P., Terroir, J.: Digital synthesis models of clarinet-like instruments including nonlinear losses in the resonator. In: the 9th International Conference on Digital Audio Effects, vol. 83 (2006). Citeseer

[34] Taillard, P.-A.: Theoretical and experimental study of the role of the reed in clarinet playing. PhD thesis, Le Mans Université (2018)